Available online at www.sciencedirect.com

European Journal of Mechanics B/Fluids 23 (2004) 551–569

Near-field pairing of leading-edge vortices in elliptic jets in cross flow

T.H. New [a], J. Soria [b,*]

[a] *ME Department, National University of Singapore, Singapore*
[b] *Laboratory for Turbulence Research in Aerospace & Combustion, ME Department, Monash University, Melbourne, VIC 3800, Australia*

Received 20 January 2003; received in revised form 6 October 2003; accepted 30 October 2003

Abstract

MCCDPIV measurements of the in-plane velocity components and out-of-plane vorticity for two elliptic jets of aspect ratio of 2 and 3 exhausting normally into a cross flow with velocity ratios ranging from 3 to 5 have been carried out. The purpose is to obtain quantitative data on the vortex pairing process which occurs along the leading edge of the cross flow/jet shear layer interface. The results show that for elliptic jets in cross flow with VR $\geqslant 3$, which have their major axis aligned in the direction of the cross flow, there is an increase in the local entrainment of the cross flow fluid during the vortex pairing.

Keywords: Elliptic jet in cross-flow; Jet in cross-flow; Multigrid CCDPIV; Vortex dynamics

1. Introduction

The study of a jet in cross flow (JICF) is important in understanding the flow physics behind various engineering applications utilizing this flow phenomenon, such as the cooling of turbine blades, combustion process, V/STOL aircraft design, missile control system and enhancement of mixing processes. Even though extensive studies have been carried out in the past few decades to investigate this phenomenon, many aspects of the flow field remain unresolved. The highly three-dimensional flow proves to be a major stumbling block in the better understanding of the overall flow field. The flow field consists of various major vortical systems interacting mutually with one another, but essentially comprise a horseshoe or necklace vortex, leading-edge vortices, a counter-rotating vortex pair (CVP) and wake vortices as illustrated schematically in Fig. 1.

While most studies on JICF phenomenon concentrated their efforts on the circular jet geometry, it is believed that jets of other geometries can also be of immense potential, especially in the area of passive mixing. Previous studies have shown that even in the free jet configuration, non-circular geometries (i.e., square, rectangular, elliptic and lobed) exhibit higher mixing rates than a circular geometry. [1] studied the conditions affecting the near-field behaviour of a subsonic square jet and followed up with a numerical study on low aspect ratio rectangular free jets [2], concentrating on the vortex dynamics' role in the near-field entrainment. The conclusion was that the near-field entrainment was related to the interaction between the ring and rib-like corner vortices, as well as the axis-switching timing. The occurrence of axis-switching for non-circular jet geometries results in an increase in the production of small-scale structures, facilitating increased entrainment. As for elliptic free jets, recent studies [3–6] determined that axis-switching also plays an important role similar to those geometries with corners, albeit without the associated corner vortices. Further information on the behaviour of non-circular jet geometries is provided in the comprehensive review of [7].

---

[*] Corresponding author.
E-mail address: julio.soria@eng.monash.edu.au (J. Soria).
URL: http://www-personal.monash.edu.au/~julio (J. Soria).

0997-7546/$ – see front matter © 2003 Elsevier SAS. All rights reserved.
doi:10.1016/j.euromechflu.2003.10.007

Nomenclature

AR	aspect ratio, dimensionless
CVP	counter-rotating vortex pair
EJICF	elliptic jet in cross flow
d_{major}	major diameter of ellipse, mm
d_{hyd}	hydraulic diameter of ellipse, mm
IW	linear PIV interrogation window size, pixel, px
JICF	jet in cross flow
L	characteristic length scale of a vorticity distribution, mm
MR	momentum ratio, dimensionless
px	pixel
Re_j	jet Reynolds number, $U_j d_{\text{hyd}}/\nu$, dimensionless
t	time, s
(u, v)	Cartesian velocity components in (x, y) Cartesian coordinates, mm/s
U_j	velocity of the jet at the jet orifice, mm/s
U_∞	uniform cross flow velocity, mm/s
VR	velocity ratio, dimensionless
x	Cartesian coordinate axis in the direction of the free-stream flow, mm
y	Cartesian coordinate axis in the direction of normal to free-stream flow, mm
Δ	discrete spatial sampling spacing between the PIV measurements, mm
λ_0	ratio of non-dimensional uncertainty in the MCCDPIV velocity measurement to non-dimensional uncertainty in vorticity, dimensionless
ρ_j	jet fluid density, kg/m^3
ρ_∞	cross flow fluid density, kg/m^3
ω_z	spanwise vorticity pointing in a direction normal to the (x, y) plane, s^{-1}
ω_{bias}	vorticity bias error, s^{-1}
ω_{exact}	exact value of the vorticity, s^{-1}

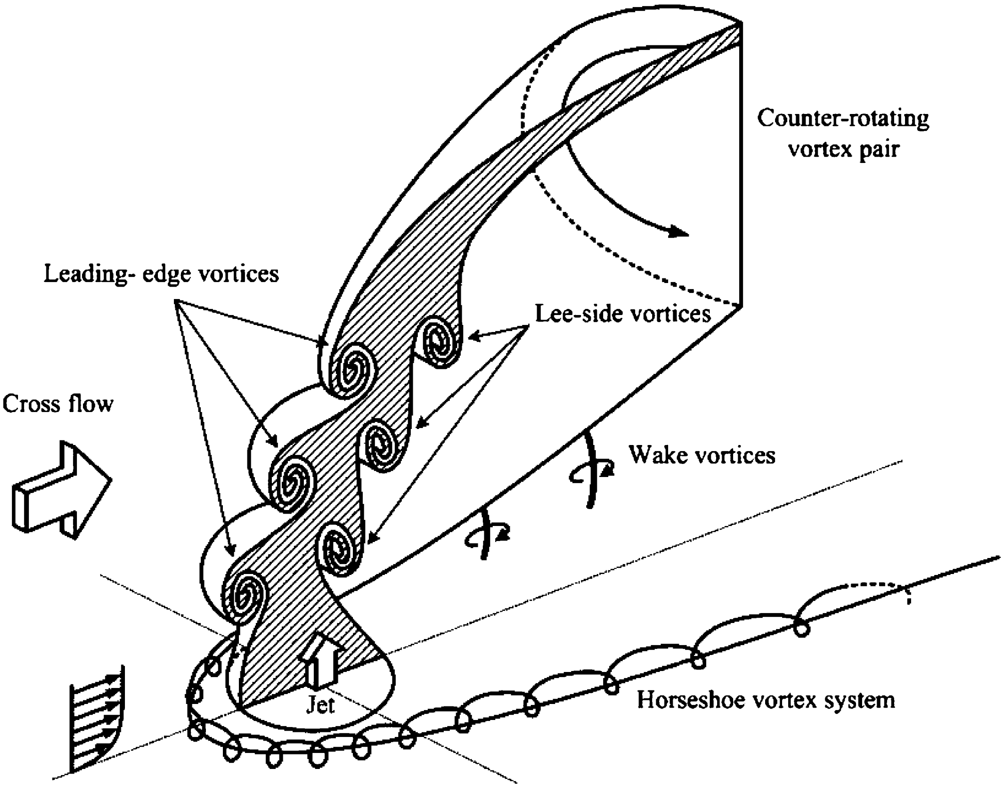

Fig. 1. A schematic illustration showing the major vortex systems resulting from a circular jet in cross flow. A cross-section view is depicted along the symmetry plane of the deflected jet to illustrate the corresponding structures.

Of the many possible jet geometries used in a cross flow environment, elliptic jets remain one of the least studied with the few exceptions of [8,9]. Furthermore, to the best of the authors' knowledge, no numerical or analytical work has been carried out for this flow configuration. In contrast, many experimental and numerical investigations have been carried out on a circular jet in cross flow, such as [10–19]. For further information on circular jets in cross flow, the reader should refer to the review by [20]. Square and rectangular jets in cross flow have also been relatively well covered by [8,9,21] due to their immediate applications in the aerospace industries. The lack of experimental information for the Elliptic Jet in Cross Flow (EJICF) has been the impetus for the present study of this flow field.

Our recent studies on EJICF (see [22,23]) have shown that with the major axis of the ellipse aligned with the cross flow, the flow field does not deviate significantly from that of circular JICF as long as VR < 3. However, for flow conditions with VR $\geqslant 3$, the vortex-pairing phenomenon of the leading-edge vortices was found to dominate the near-field. Interestingly, no such phenomenon was found when the elliptic jets are aligned in the blunt orientation. Fig. 2 shows two instances of flow visualization where pairing occurred. Therefore, the motivation of this study is to investigate quantitatively the leading-edge vortex-pairing phenomenon exhibited by streamwise EJICF when the VR $\geqslant 3$ through a series of PIV measurements. While this might not be the first time that such vortex-pairing events have been reported for JICF, the strong self-induction and sustained behaviour of vortex-pairing without any need for external input makes the EJICF very promising for increased mixing.

2. Experimental apparatus

The experiments were carried out in the recirculating water tunnel in the Fluid Mechanics Laboratory of the National University of Singapore. The test section, which measures 1.83 m in length and 0.4 m by 0.4 m in cross-section, is fabricated of Plexiglas to allow easy high-quality flow visualization and measurement. Two elliptic jets of AR = 2 and 3, having lengths of major and minor axes of 45 mm and 22.5 mm and 55.5 mm and 18.5 mm respectively, are considered here. The dimensions are selected such that both the elliptic jet exits have the same cross-section areas. A small quantity of water from the water tunnel is constantly being channeled into an overhead water tank to provide the fluid for the jets. The exit of the jet assembly is flush-mounted to the test section floor. A variable speed pump is used to drive the cross flow water in the test-section, and

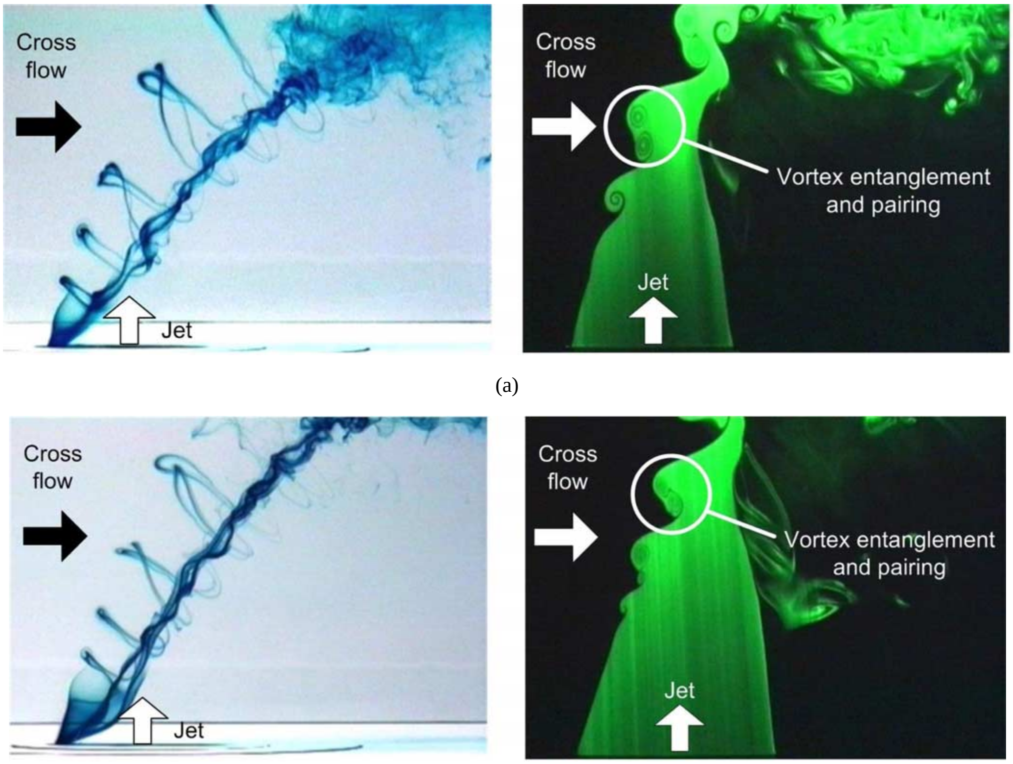

(a)

(b)

Fig. 2. Dye and laser induced fluorescence flow visualisations showing regular vortex pairing behaviour exhibited by the streamwise AR = 2 and 3 EJICF at VR = 3. Dye flow visualisation shows the three-dimensional vortex loops emanating from the interaction between the jet and cross flow, while the laser induced fluorescence visualisations reveal the details of the entanglement and pairing process of the vortex loops. (a) Streamwise AR = 2, (b) streamwise AR = 3.

before the water is recirculated back into the test section, it is passed through a honeycomb grid and three layers of fine screens with decreasing mesh sizes. This is to ensure that the turbulence level of the cross flow remains low in the test-section. All flow rates are measured using electromagnetic flow meters and relevant velocities are obtained by dividing the time-averaged volume flow rates by the relevant jet cross-sectional areas. One of the important parameters in the present study is the momentum ratio, which is the ratio of the jet momentum flux to the cross flow momentum flux over the same jet cross-sectional area, which can be written as

$$\text{Momentum Ratio} = \text{MR} = \frac{\int \rho_j U_j^2 \, \mathrm{d}A}{\rho_\infty U_\infty^2 A_j}, \tag{1}$$

where ρ_j, U_j and A_j are the density, velocity and cross-sectional area of the jet at the orifice exit respectively, and ρ_∞ and U_∞ are the corresponding density and velocity of the uniform cross flow respectively. However, when both jet and cross flow fluids have the same density, this ratio simplifies to one of the mean jet velocity to mean cross flow velocity, which is conventionally referred to as the velocity ratio,

$$\text{Velocity Ratio} = \text{VR} = \frac{U_j}{U_\infty}. \tag{2}$$

The jet apparatus was constructed in such a way that the exhausting jet tubes could be rotated relatively to the attachment fixed to the water tunnel test-section floor. To ensure a high rotational resolution and accurate alignment of the jet orientations, worm-gears were used for fine adjustments of the jet orifice position as shown in Fig. 3(a). While the jet orifices can be rotated to assume any orientation, only the streamwise orientation was investigated in the present study. Here, streamwise orientation is the case when the major-axis of the elliptic jet is aligned parallel with the oncoming cross flow, and the blunt configuration is the case when the minor-axis of the elliptic jet is aligned parallel with the cross flow (see Fig. 3(b)). In all cases, the cross flow velocity was maintained constant at 30 mm/s and the velocity ratios were achieved by adjusting the jet flow rates. Jet Reynolds number based on the hydraulic diameter varied slightly between the two elliptic jets as the dimensions were different despite having the same jet exit cross-section areas. For the AR = 2 elliptic jet, Re_j varied between 3054 and 5090, whereas for the AR = 3 elliptic jet, Re_j ranged from 2663 to 4439.

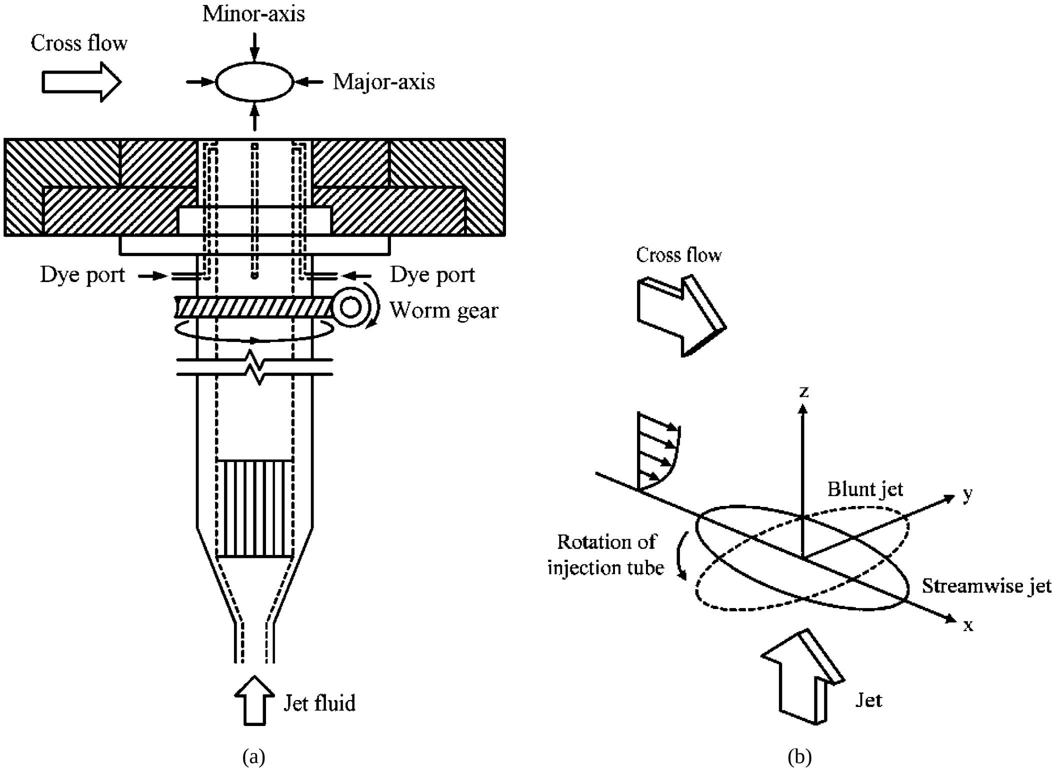

(a) (b)

Fig. 3. Precise alignment of both elliptic jets is accomplished by a worm-gear setup attached to the rotatable jet tube as illustrated in (a). Streamwise and blunt orientations are depicted in (b) with respect to the cross flow. (a) Jet apparatus, (b) streamwise and blunt orientations.

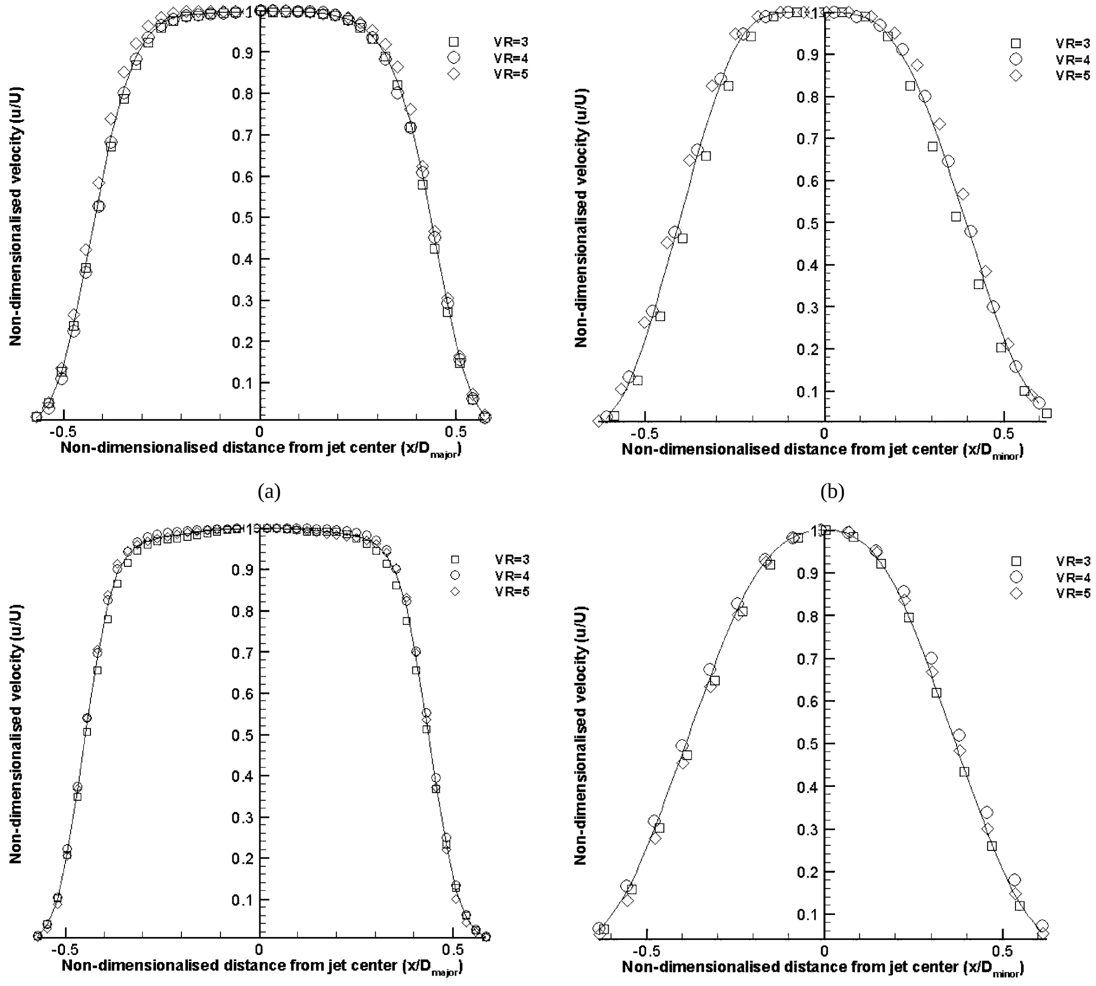

(a) (b)

(c) (d)

Fig. 4. Non-dimensionalised velocity profiles for the AR = 2 and 3 elliptic jets in free jet configuration at velocities used for VR = 3–5. (a) AR = 2 major-axis, (b) AR = 2 minor-axis, (c) AR = 3 major-axis, (d) AR = 3 minor-axis.

Before carrying out the PIV measurements, the jet exit velocity profiles in the absence of the cross flow were measured using a Dantec 55R11 single-sensor hot-film probe together with a constant temperature anemometer. The probe was traversed approximately 1 mm above and across the major and minor diameters of the two elliptic jets for each of the velocity ratios of 3 to 5. The hot-film signal was DC offset and low-pass filtered at 5 kHz. The post-processed signal was amplified by 10 dB to arrive at the final signal that was digitally recorded. The digital sampling frequency for the hot-film signal was set at 1 kHz and a total of 30 000 velocity measurement samples were taken at each measurement point. Fig. 4 shows the mean jet exit velocity profiles measured across the major- and minor-axis of the elliptic jet, which demonstrates the presence of top-hat velocity profiles along the streamwise configuration for all the velocity ratios used in the present study.

3. PIV image acquisition

Low and high-spatial resolution PIV measurements were carried out on the two EJICFs with the intended velocity ratios. The former allowed not only an appreciation of the overall flow structure before the operating parameters of high-spatial resolution PIV measurements were decided, but also provided information of the temporally-resolved vortex dynamics evolution. For the present experiments, the laser light sheets were orientated such that they passed through the centerline of the deflected jets in the cross flow direction. The experimental details of these low-spatial resolution PIV measurements are provided in Table 1. The single-exposed image pairs were analysed with cross-correlation DPIV [24,25].

For the high-spatial resolution PIV measurements, the flow regions of interest were divided into two overlapping parts as shown in Fig. 5. The two parts, each covering 45 mm × 45 mm in physical size, were cascaded vertically with 14 mm of vertical overlap. A distance of 22.5 mm separated the jet exit and the lower edge of the lower Window 1. The two parts were selected to cover the entire leading-edge jet shear layers, where production and subsequent downstream convection of the leading-edge vortices occurs continuously. The experimental details of the high-spatial resolution PIV measurements are provided in Table 1. Triggering and co-ordination of the Nd:YAG laser, as well as the CCD camera exposure time was controlled by a PC. To achieve

Table 1
PIV experimental details

	Low spatial resolution PIV experiments	High spatial resolution PIV experiments
Seeding:		
diameter [µm]	60	30
ρ [kg/m^3]	1000 ± 20	1000 ± 20
Seeding density [particles/IW]	>10	≈10
Illumination:	Continuuin Nd:YAG twin cavity laser	Continuuin Nd:YAG twin cavity laser
Max. Power per pulse [mJ]	200	200
Pulse width [ns]	8	8
Max. repettion rate [Hz]	10	10
Laser sheet thickness [mm]	2	2
CCD details:	Kodak ES 1.0	Roper ES 4.0
Array size [px^2]	1024^2	2048^2
Signal digitisation [bits]	8	12
Image pair acquisition frequency [Hz]	10	2.5
PIV analysis:	CCDPIV	MCCDPIV
$\frac{\Delta}{d_{\mathrm{major}}}$	0.031	0.006 (AR = 3)–0.008 (AR = 2)
$\frac{IW}{d_{\mathrm{major}}}$	0.031	0.006 (AR = 3)–0.008 (AR = 2)
Spurious vectors [%]	≈10	≈5

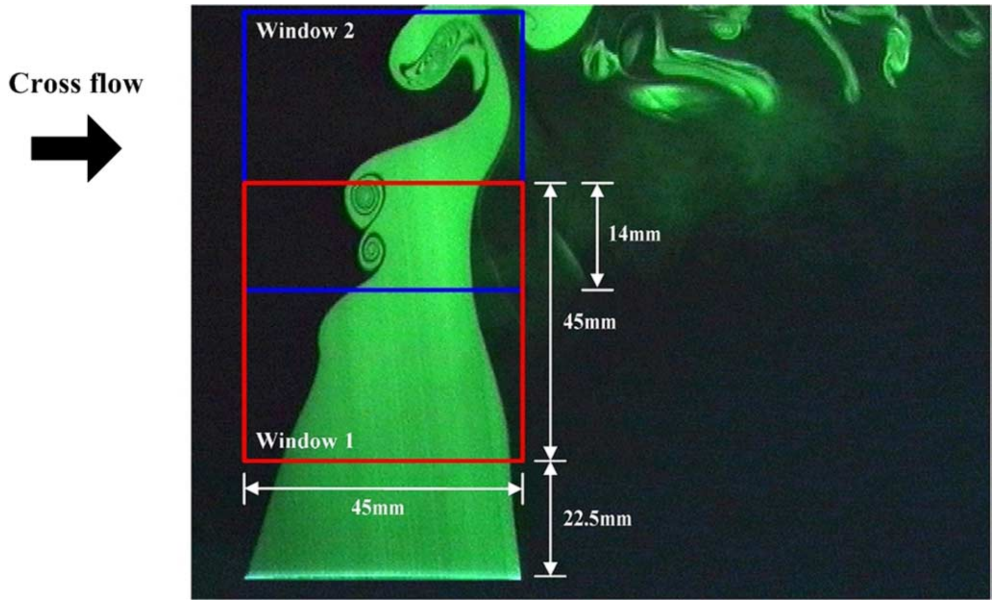

Fig. 5. The regions of interest for the high-spatial resolution MCCDPIV measurements. Each smaller region, or window, covers a physical area of 45 mm × 45 mm and the size of the overlapping region was 14 mm × 45 mm. The distance between the jet exit and lower window was 22.5 mm.

a high degree of accuracy of the triggering timings, Real-Time Linux (RTAI) was used with an in-house developed program that produced the necessary TTL signals through the parallel port of the PC. These single exposed image pairs were analysed using the multigrid cross-correlation digital PIV (MCCDPIV) algorithm described in [26], which has its origin in an iterative and adaptive cross-correlation algorithm introduced by Soria [27,28] and [29,27]). Details of the performance, precision and experimental uncertainty of the MCCDPIV algorithm with applications to the analysis of single exposed PIV and holographic PIV (HPIV) images have been reported in [30,31], respectively.

The high-spatial resolution PIV experiments were designed for a two-pass MCCDPIV analysis. The first pass used an IW = 64 px, while the second pass used an IW = 32 px with discrete IW offset to minimize the measurement uncertainty [32]. The sampling spacing between the centres of the interrogation windows was 16 px. The MCCDPIV algorithm uses the local cross-correlation function multiplication method introduced by [33] to improve the search for the location of the maximum value of the cross-correlation function. For the sub-pixel peak calculation, a two dimensional Gaussian function model was used to find, in a least square sense, the location of the maximum of the cross-correlation function [27]. The MCCDPIV data field was subsequently validated with a global histogram operator check [34], a median test [35], and by applying the dynamic mean value operator test described in [34]. The tests were applied in the specified order. Following data validation, the in-plane velocity components (u, v) in the (x, y) coordinate directions respectively were computed by taking the optical magnification into account and by dividing the measured MCCDPIV displacement in each interrogation window by the time between the exposures of the image pair. The x coordinate direction is taken as the free-stream direction, while the y direction is the cross-stream direction. The uncertainty relative to the maximum velocity in the velocity components at the 95% confidence level for these measurements is 0.3%.

4. Vorticity calculation

The out-of-plane vorticity, ω_z, was calculated from the MCCDPIV velocity field measurements using a local least-squares fit procedure to the velocity field, followed by analytic differentiation using the relationship

$$\omega_z = \frac{\partial v}{\partial x} - \frac{\partial u}{\partial y}. \tag{3}$$

A thirteen point, two-dimensional, local fit to the data was used [29]. This calculation is an approximation that introduces additional bias and random error into the vorticity value. These errors have been investigated and discussed in [36]. The ratio of the biased vorticity error, ω_{bias}, to the exact value of the vorticity, ω_{exact}, shown in Eq. (4) can be derived using the methodology outlined in [36] and can be used to estimate the biased vorticity error.

$$\frac{\omega_{\text{bias}}}{\omega_{\text{exact}}} = -0.7478\left(\frac{\Delta}{L}\right)^{1.96}. \tag{4}$$

This relationship shows that the bias error is related to the sampling separation between velocity measurements, Δ. The parameter L can be thought of as being a characteristic length scale of the vorticity distribution.

The ratio of the random error in the MCCDPIV velocity measurement compared to ω_z is denoted by λ_0 and can be calculated using the relationship derived in [36] shown in Eq. (5). This relation is specific to the thirteen point fitting technique used to calculate the vorticity.

$$\lambda_0 = \sqrt{\frac{1}{5}}\left(\frac{L}{\Delta}\right). \tag{5}$$

For a vorticity distribution with a characteristic length scale of 16Δ, the bias error is estimated as -0.3% and the random error is estimated as $\pm 2.4\%$ at the 95% confidence level, while for a vorticity distribution with a characteristic length scale of 4Δ, the bias error is estimated as -4.9% and the random error is estimated as $\pm 0.6\%$ at the 95% confidence level.

5. Results and discussion

5.1. Low-spatial resolution temporally-resolved CCDPIV measurements

Figs. 6 and 7 show the temporally-resolved out-of-plane vorticity fields associated with the leading-edge vortex-pairing behaviour of AR = 2 and 3 streamwise EJICF when the velocity ratio is 4 and 3 respectively. While vortex-pairing behaviour is prevalent for velocity ratios higher than these for each elliptic jet, only a single representative case is shown here for each elliptic jet for brevity. These figures were obtained at a low magnification factor of approximately 11, which cover a horizontal distance

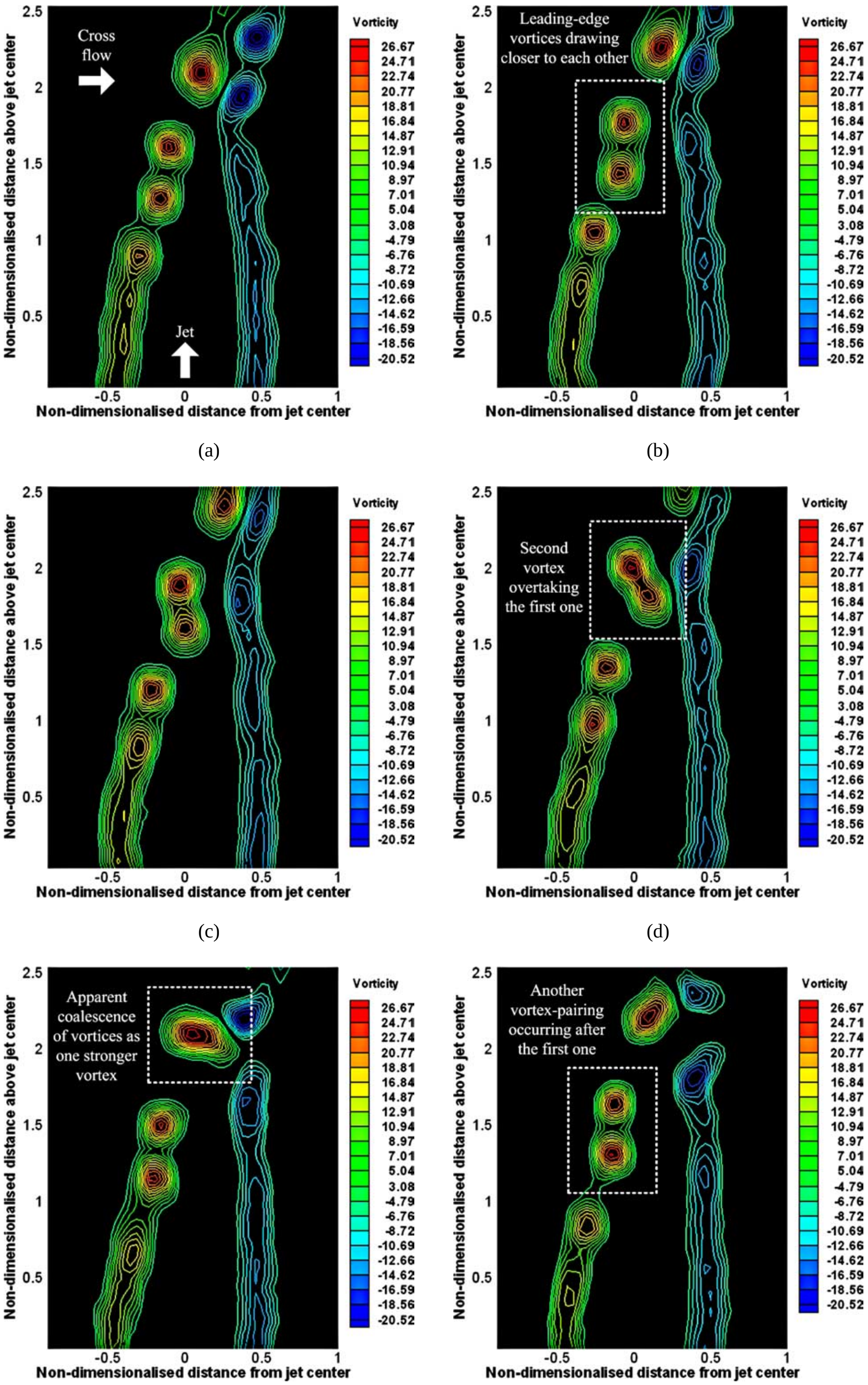

(a) (b)

(c) (d)

(e) (f)

Fig. 6. A sequence of vorticity contour plots showing the self-repeating pairing process of the leading-edge vortices for a streamwise AR = 2 EJICF at VR = 4. The first vorticity field is arbitrarily set to $t = 0.0$ s and the fields are separated by 0.1 s. (a) $t = 0.0$ s, (b) $t = 0.1$ s, (c) $t = 0.2$ s, (d) $t = 0.3$ s, (e) $t = 0.4$ s, (f) $t = 0.5$ s.

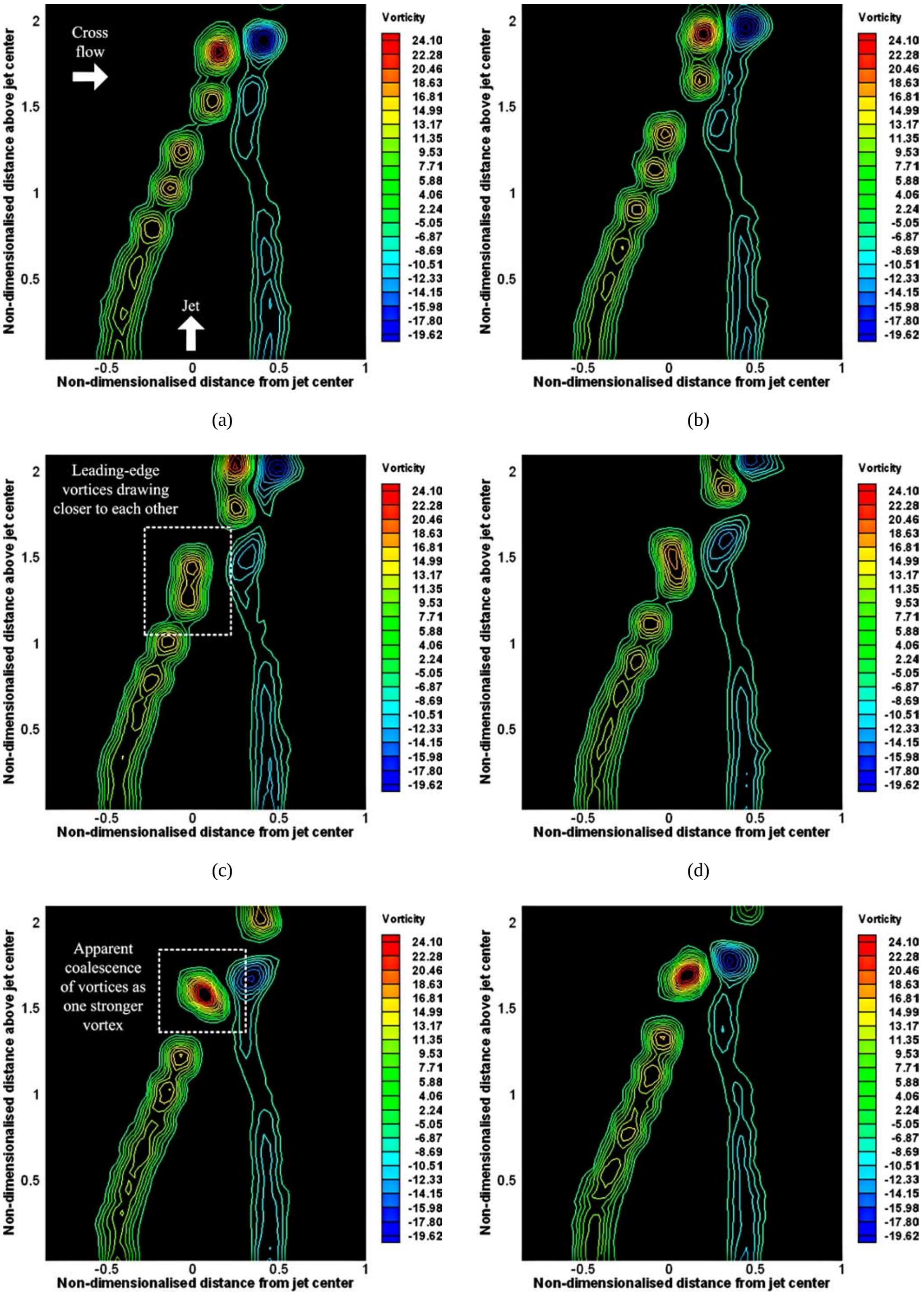

(a) (b)

(c) (d)

(e) (f)

Fig. 7. A sequence of vorticity contour plots showing the self-repeating pairing process of the leading-edge vortices for a streamwise AR $= 3$ EJICF at VR $= 3$. The first vorticity field is arbitrarily set to $t = 0.0$ s and the fields are separated by 0.1 s. (a) $t = 0.0$ s, (b) $t = 0.1$ s, (c) $t = 0.2$ s, (d) $t = 0.3$ s, (e) $t = 0.4$ s, (f) $t = 0.5$ s.

of approximately 2 times the elliptic jet major-diameter axis and a vertical distance of between 2 to 2.5 major-diameter axis above the jet orifice. The figures are 0.1 s apart with the first one arbitrarily set to $t = 0.0$ s. Cross flow is shown conventionally as going from left to right with the jets emerging vertically from the horizontal x-axes where the jet orifices coincide. It has been previously shown that for circular JICF, the leading-edge jet shear layers were observed to shed leading-edge vortices regularly due to the interaction with the oncoming cross flow. These vortices continue to convect downstream along the cross flow/jet shear layer interface of the deflected jets until transiting to turbulence. For the streamwise EJICF of both the aspect

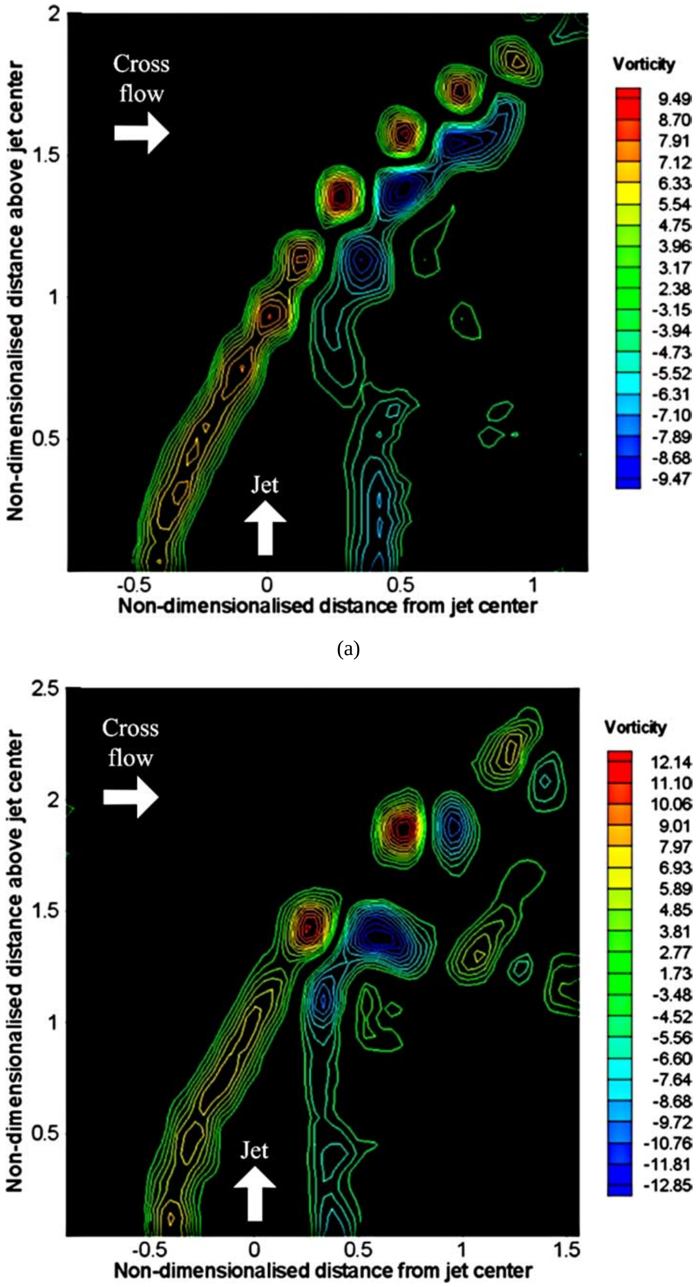

(b)

Fig. 8. Vorticity contour plots for velocity ratios less than three (VR = 2 in this case) – no vortex-pairing behaviour is observed. Leading-edge vortices, depicted as regions of concentrated vorticity of positive magnitude, convect downstream as distinct vortices, undisturbed by any flow anomalies until transiting to turbulence further downstream. (a) AR = 2 EJICF, VR = 2, (b) AR = 3 EJICF, VR = 2.

ratios studied here, when the velocity ratios are approximately less than 3 (e.g., VR = 2), the shed leading-edge vortices remain distinct individual concentrated vortices along the upstream jet shear layers as shown in Fig. 8. This structure was observed up to 2 to 2.5 elliptic jet diameters above the jet exit, depending on the actual experimental conditions. However, when the velocity ratio is 3 or higher as illustrated in the temporal out-of-plane vorticity field evolutions shown in Figs. 6 and 7, the leading-edge vortices do not have the same structure as those in the lower velocity ratio jet. Instead, shortly after the inception of individual leading-edge vortices, pairs of these vortices draw closer to each other due to mutual interaction, and eventually pair-up as they convect downstream. The vorticity fields seem to support the notion that the “entangling” of the leading-edge vortices is a direct result of the jet orifice geometry. Previous experimental studies on free elliptic jets exiting into a quiescent environment by [6] have established that the shear layer vortices along the major-plane (i.e., datum plane along the major-diameter axis) undergo similar regular pairing. They attributed this phenomenon to the distribution of dissimilar self-induced velocities along the entire elliptic vortex ring caused by the continuously changing curvature of the elliptic jet orifice. Although no evidence of vortex rings was found in EJICF, mutual interaction of the leading edge vortices was found to lead to a similar pairing process. While the PIV results in Figs. 6 and 7 give a global perspective of the pairing process, much of the detailed flow structure cannot be resolved. To address this shortcoming, a high-spatial resolution MCCDPIV study was subsequently carried out, and the results obtained are reported in the next section.

5.2. High-spatial resolution MCCDPIV measurements

Typical velocity vector fields for the two windows obtained from high-spatial resolution MCCDPIV measurements are shown in Figs. 9 and 10 for AR = 2 and 3, respectively. Due to the higher number of velocity vectors available in these vector fields, only every second vector in each direction is shown. Furthermore, the vectors are shown in colour to reflect the out-of-plane vorticity level, which shows the regions of concentrated vorticity representative of leading-edge vortices that are evolving along the upstream jet shear layer. It is worth noting that the velocity vector fields were shown with reference to Window 1 and 2 and that these windows are not related temporally but rather, spatially.

With reference to Fig. 9 for the AR = 2 EJICF, Window 1 shows the regular shedding of the leading-edge vortices without undergoing vortex pairing from VR = 3 to 5. However, the shear layer instabilities seem to be more manifest and convect more readily as the velocity ratio increases, as can be seen in the decreasing distances between individual vortices as the velocity ratio increases. This higher shedding and convection rate also suggests the additional possibility that the vortices would suffer higher flow distortion, and the velocity vector field for VR = 5 seems to support this supposition with its slightly more disrupted velocity field along the leading-edge jet shear layer. Proceeding to Window 2 however, regular vortex-pairing can now be observed very clearly. Hence, it is observed that for the AR = 2 EJICF, leading-edge vortex-pairing usually occurs at least $1.5d_{\mathrm{major}}$ vertically above the jet orifice. This distance is inferred by comparing the figures where vortex-pairing occurs and the window positions in Fig. 9. In addition to providing support for the vortex-pairing behaviour, the velocity vector fields also strongly suggest that with each vortex-pairing, there is a sudden surge in the local entrainment of the cross flow fluid into the main jet body via the cross flow/jet shear layer interface.

With few exceptions, the general flow features remain unchanged for the AR = 3 EJICF shown in Fig. 10. Firstly, vortex-pairing is observed even in Window 1. This is different from the corresponding AR = 2 EJICF case and suggests that the jet geometry is responsible for this structural deviation. It is therefore not surprising that vortex-pairing is in an advanced stage of progress in Window 2 for all velocity ratios. The location where vortex-pairing is initiated is approximately $0.5d_{\mathrm{major}}$ to $1.0d_{\mathrm{major}}$ above the jet orifice. Secondly, subsequent entrainment and penetration of the paired vortices into the main jet body for the case of AR = 3 EJICF is less than the corresponding one for the AR = 2 EJICF. While not very clearly illustrated in the above velocity vector fields, it was often visually observed during the experiments that the leading-edge vortices shed by the AR = 3 EJICF were qualitatively smaller than those of the AR = 2 EJICF. There are several possible explanations for this. Firstly, relating this observation with the velocity profiles across the major-planes of the AR = 2 and 3 elliptic jets in a free jet configuration, the comparatively thinner jet boundary layer at the leading-edge of the AR = 3 EJICF seems to limit the scale of the leading-edge vortices. Secondly, the self-induced velocities at the leading-edge portions of the leading-edge vortices might cause the vortices to convect downstream faster than they can penetrate the main jet body. There are occasions though, when vortex-pairing involved three leading-edge vortices (i.e., vortex-tripling) for AR = 3 EJICF at higher velocity ratios (see Fig. 11). However, it is worthwhile noting that all the velocity fields presented here are relative to a stationary observer, which explains why some of the vortices in Fig. 11 are not so obvious, even though they show up very clearly in the vorticity plot. Even in these situations, the penetration into the main jet body is still not comparable with the AR = 2 EJICF configuration. Further work is required to resolve the issue of whether vortex-tripling can yield deeper penetration as the results obtained in the present study are unable substantiate this claim.

Figs. 12–14 show the structural changes in the velocity vector and vorticity fields during a typical vortex-pairing event. It is worth recalling that the current image pair acquisition rate does not actually permit the successive capturing of such a sequence, as the shedding frequencies of the leading-edge vortices are generally much higher than the 2.5 Hz image pair acquisition rate.

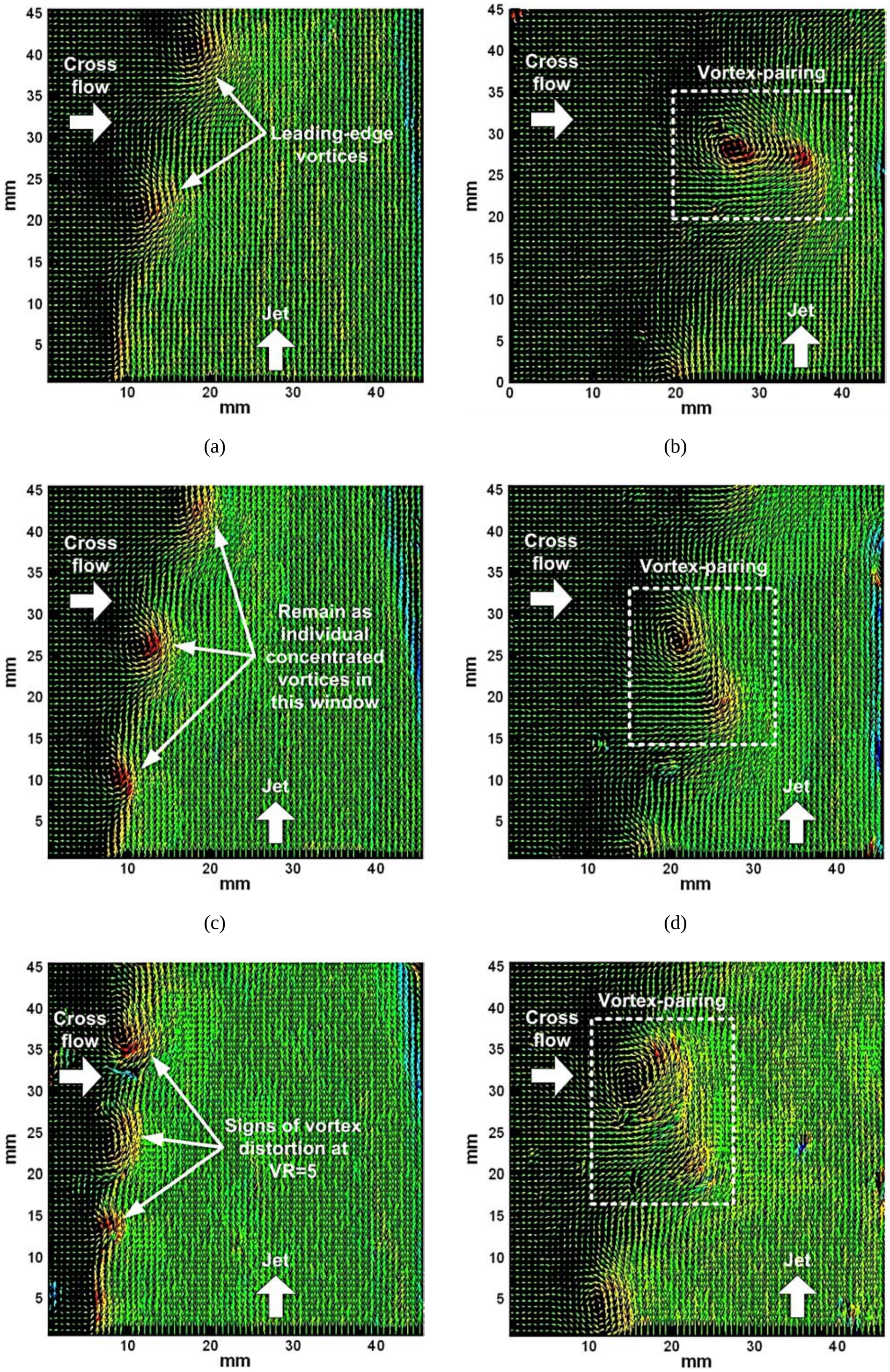

(a) (b)

(c) (d)

(e) (f)

Fig. 9. High-spatial resolution MCCDPIV velocity field measurements for AR = 2 streamwise elliptic jet at VR = 3–5 in both Windows P1 and P2. Velocity vectors are coloured with out-of-plane vorticity, red represents positive vorticity, blue represents negative vorticity. (a) AR = 2, VR = 3, Window P1, (b) AR = 2, VR = 3, Window P2, (c) AR = 2, VR = 4, Window P1, (d) AR = 2, VR = 4, Window P2, (e) AR = 2, VR = 5, Window P1, (f) AR = 2, VR = 5, Window P2.

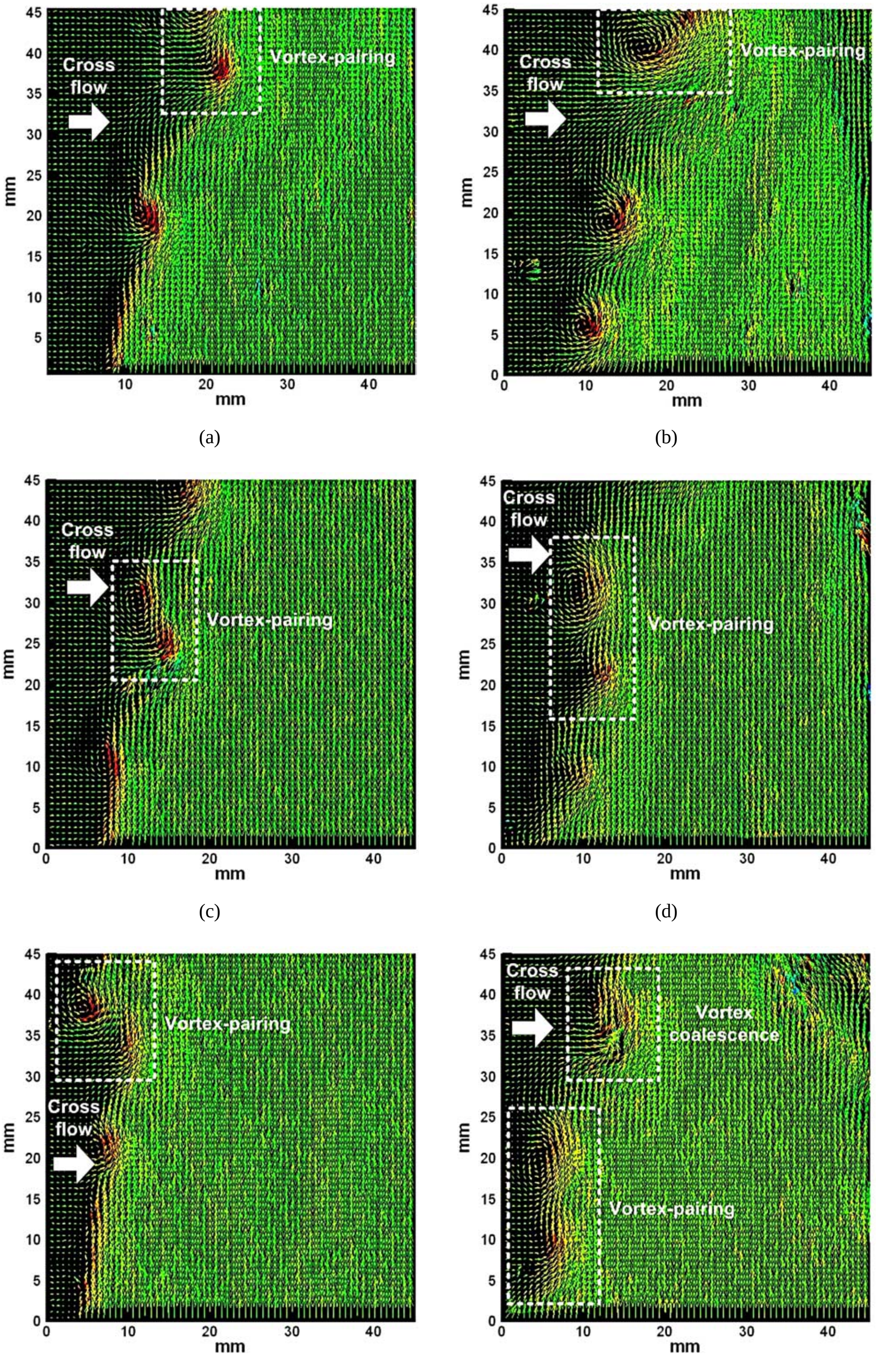

(a) (b)

(c) (d)

(e) (f)

Fig. 10. High-spatial resolution MCCDPIV measurements for AR = 3 streamwise EJICF with VR = 3–5 in both Windows 1 and 2. Velocity vectors are coloured with out-of-plane vorticity, red represents positive vorticity, blue represents negative vorticity. (a) AR = 3, VR = 3, Window P1, (b) AR = 3, VR = 3, Window P2, (c) AR = 3, VR = 4, Window P1, (d) AR = 3, VR = 4, Window P2, (e) AR = 3, VR = 5, Window P1, (f) AR = 3, VR = 5, Window P2.

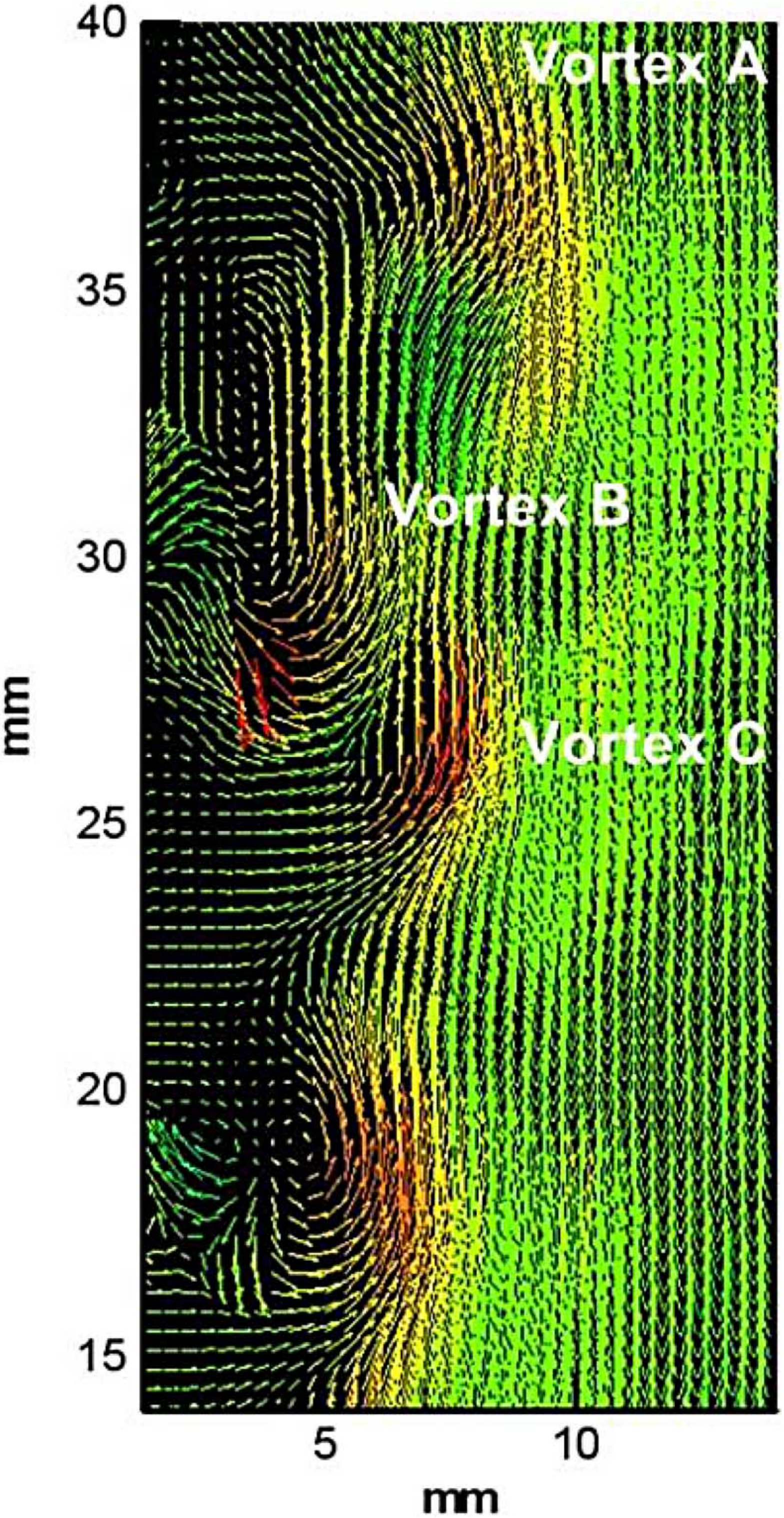

Fig. 11. Example of occasional triple vortex-pairing along the leading-edge region for AR = 3 streamwise elliptic jet at VR = 5. This phenomenon points to the high vortex-stretching levels conferred upon the leading-edge vortices due to both the action of the cross flow as well as the jet geometry.

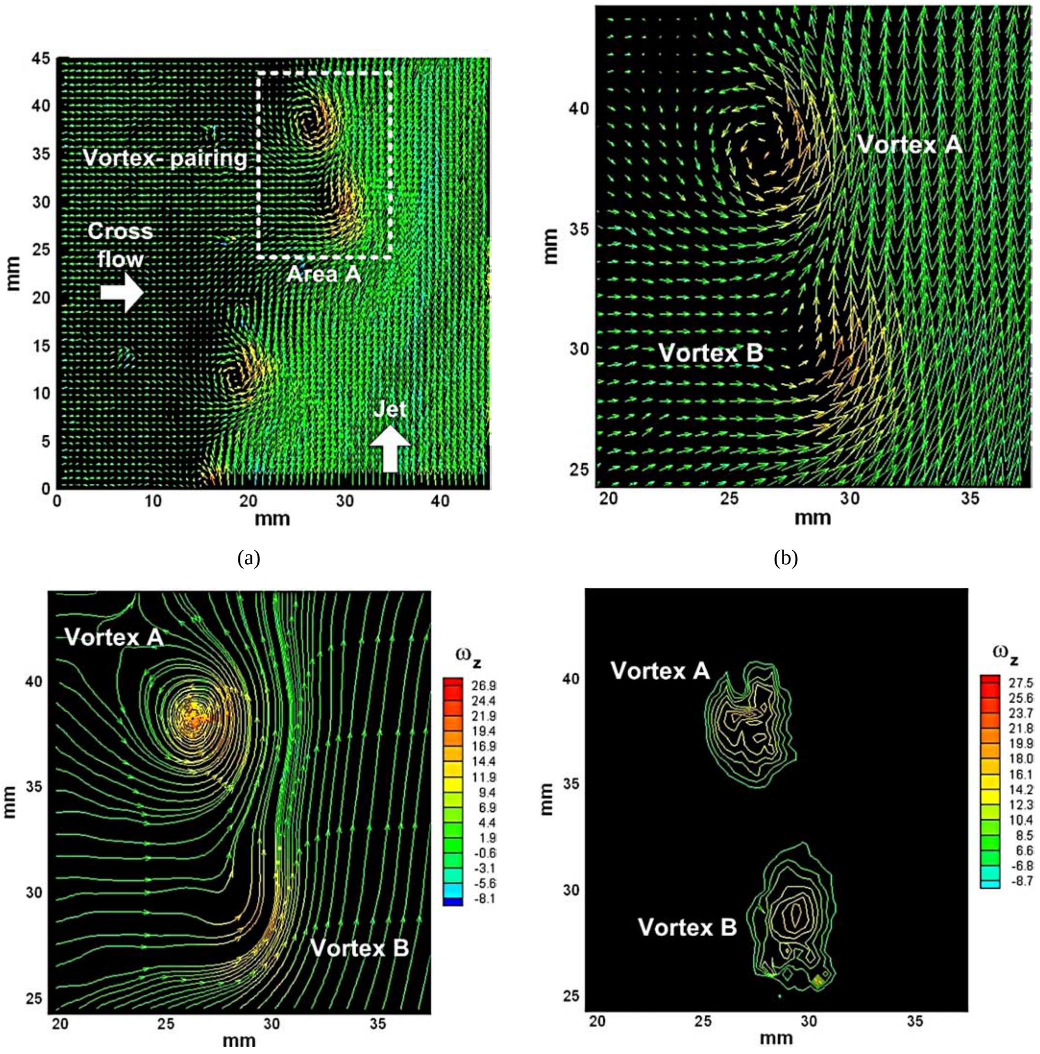

(a) (b)

(c) (d)

Fig. 12. High-spatial resolution MCCDPIV in-plane velocity field, instantaneous in-plane streamline pattern and out-of-plane vorticity for a pair of closely-spaced leading-edge vortices that are about to undergo pairing for AR = 3, VR = 3 streamwise elliptic jet. (a) Window 2, (b) instantaneous velocity field of Area A, (c) instantaneous streamlines in Area A, (d) instantaneous vorticity levels in Area A.

These two figures were in fact separated by a few image pairs, but the high repeatability of the vortex-pairings at approximately the same phase allowed a satisfactory reconstruction of a typical pairing event. Considering Fig. 12(a), where the global velocity vector field for Window 2 is shown, shedding of leading-edge vortices and subsequent gradual catching-up of the first vortex (Vortex A) by the second vortex (Vortex B) of the pair involved is clearly observed. In fact, the large numbers of velocity vectors available make it impractical to display all of them, hence every second vector in each direction is not shown. However due to the original high density of the velocity vectors, it is possible to zoom further into the region just around and including the vortices involved in the pairing process. Clearly, the vortices are in the early stages of the pairing, as can be observed from Figs. 12(b)–(d). As previously discussed, the pairing initiated with Vortex B moving to the lee-side of Vortex A and the role of Vortex A in attracting Vortex B can be detected readily in the velocity vector field. The instantaneous streamlines support this notion as well. The observation that Vortex A remains almost unperturbed when Vortex B begins to move to the lee-side (see Fig. 12 (b) and (c)) suggests that the motion of Vortex B is, in addition to its self-induced velocity at the highly-curved portion of the vortex filament (which was the leading-edge vortex), is also affected by the induced velocity field of Vortex A. Similarly, the behaviour of Vortex A is a result of the combined effect of its own self-induced velocity and the induced velocity field of Vortex B. Strictly speaking, Vortices A and B are under the influences of other flow structures as well. However, in this case the

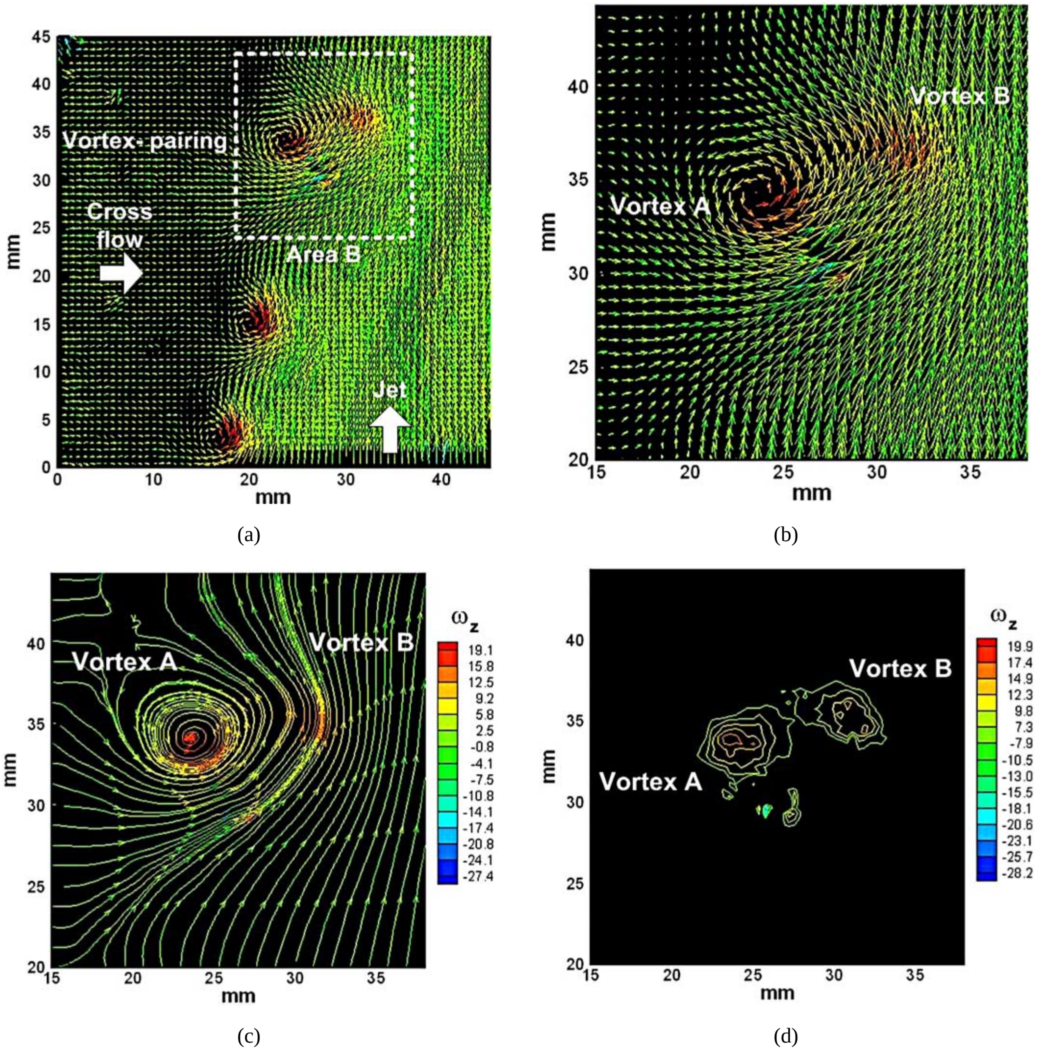

Fig. 13. High-spatial resolution MCCDPIV in-plane velocity field, instantaneous in-plane streamline pattern and out-of-plane vorticity for a pair of closely-spaced leading-edge vortices that are undergoing pairing halfway for AR = 3, VR = 3 streamwise elliptic jet. (a) Window 2, (b) instantaneous velocity field of Area B, (c) instantaneous streamlines in Area B, (d) instantaneous vorticity levels in Area B.

vortices are so close to each other that their mutual interaction will probably dominate over the other external influences. Hence, it is sufficient to consider the vortex-pairing process to stem mainly from this interaction. Fig. 12 (b) and (c) further indicate that the motion of Vortex B seems to be drawing in higher than the usual levels of cross flow fluid into the main jet body as it pulls itself inward into the jet body to overtake Vortex A from the lee-side. This produces a sudden increase in the entrainment of the cross flow fluid by the jet, as shown in the global velocity field of Fig. 12(a) and instantaneous streamlines in Fig. 12(c). At this point in time, however, the two leading-edge vortices remain distinct and largely undistorted as shown in Fig. 12(d).

Fig. 13 shows the flow field at a slightly later time for the pair of vortices in Fig. 12, and Fig. 13(a) depicts the scenario where Vortex B has just overtaken Vortex A and is about to proceed to entangle it further. Vortex B seems to have suffered higher levels of stretching when it overtook Vortex A from the lee-side and furthermore, the stretching couple of the induced velocity from Vortex A also caused Vortex B to wrap partially around Vortex A. Along with the vortex pairing is the continuing increase in the cross flow fluid entrainment in this vicinity, as is evident in the data shown in Fig. 13 (b) and (c) and suggested previously by Fig. 12. At this instance, however, the increase in the entrainment is evident from the instantaneous streamline pattern shown in Fig. 13(c). It is worth noting that the entrainment is defined here as the “engulfing” of the oncoming cross flow fluid across the cross flow/leading-edge jet shear layer interface caused by the generation of the leading-edge vortices. This definition is based on a two-dimensional view of the flow field, and while it appears somewhat simplistic, it is sufficient for the

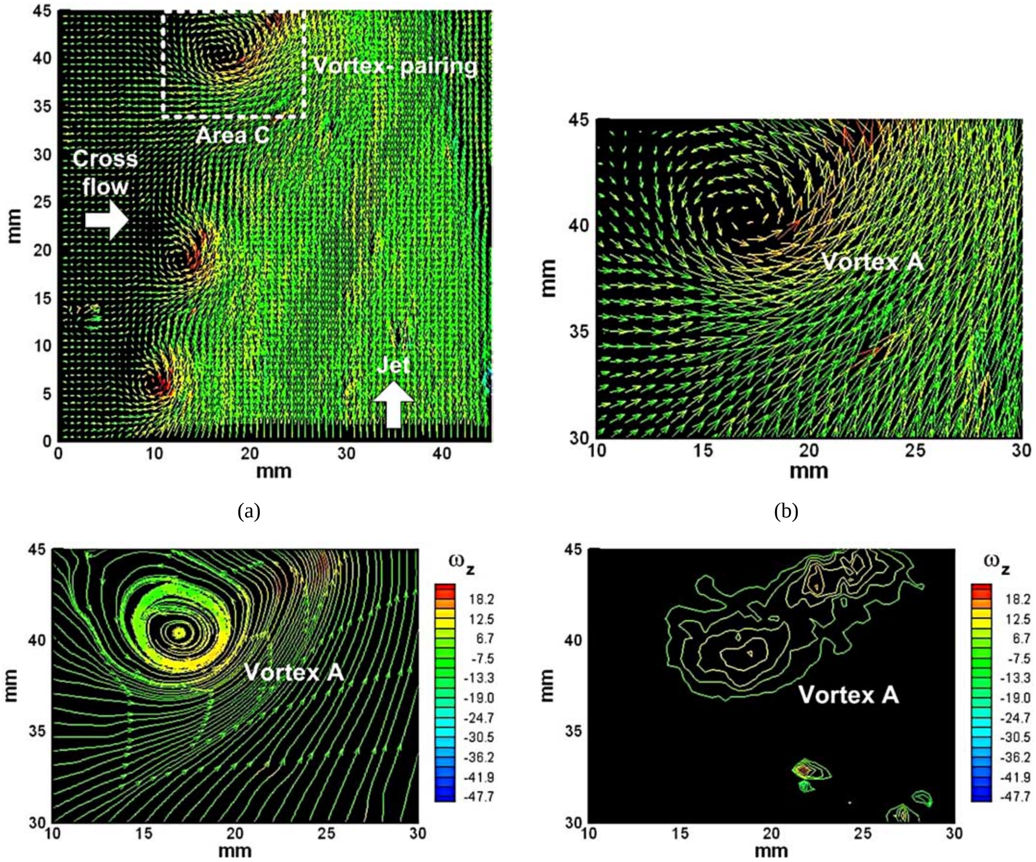

(a) (b)

(c) (d)

Fig. 14. High-spatial resolution MCCDPIV in-plane velocity field, instantaneous in-plane streamline pattern and out-of-plane vorticity for a pair of closely-spaced leading-edge vortices that are undergoing pairing halfway for AR = 3, VR = 3 streamwise elliptic jet. (a) Window 2, (b) instantaneous velocity field of Area C, (c) instantaneous streamlines in Area C, (d) instantaneous vorticity levels in Area C.

discussion here. As the two vortices draw closer to each other, the concentrated vorticity that was Vortices A and B shown in Fig. 13(d) also begins to show signs of distortion (compare Fig. 13 to Fig. 12).

Fig. 14 shows the further development of these vortices. At this point in time, the two merged vortices can be virtually regarded as a single vortex. Unlike Figs. 12 and 13, where the vortices can still be seen as mostly individual vortex structures, albeit under severe flow straining, Fig. 14 marks the beginning of their entanglement for subsequent coalescence into a single vortex entity. Here,the velocity vector fields and instantaneous streamlines also continue to show the increasing inflow of cross flow fluid into the leading-edge region of the jet shear layer, lending credence to the notion that such phenomenon can be useful for further mixing improvement.

6. Concluding remarks

A low-spatial resolution as well as a high-spatial resolution MCCDPIV study has been carried out for two elliptic jets of AR = 2 and 3 exhausting normally into a cross flow with velocity ratios ranging from 3 to 5. Within the flow conditions used in the present study, coherent vortex-pairing of the leading-edge vortices are found to occur periodically along the cross flow/leading-edge jet shear layer even though no deliberate external forcing is applied. The pairing process is a result of the mutual interaction between adjacent vortices. It was observed that during the vortex-pairing an abrupt surge of the cross flow fluid into the main jet body occurs wherever vortex-pairing begins, suggesting a corresponding increase in the local entrainment surrounding the paired-vortices. The vortex-pairing process was found to have begun with the upstream vortex of the two involved leading-edge vortices undergoing a sudden overtaking of the downstream vortex from its lee-side. Under the induced action of the downstream vortex as well as its own self-induction, the upstream vortex then subsequently "entangles" the downstream vortex. The entanglement of the leading-edge vortices was confirmed by the high data resolution of the DPIV measurements, where the upstream vortex was clearly found to "wrap" around the downstream vortex before both vortices coalesced together. While previous low-spatial resolution studies were able to capture the occurrence of the phenomenon, it was the present high-spatial resolution experimental results which revealed that the "overtaking" vortex usually undergoes a much larger change in its topology than the one being "overtaken" (the downstream vortex). The state of the downstream vortex remained largely unchanged until the later stages while the upstream vortex suffers immediate high levels of distortion, probably due to numerous occurrences of vortex-stretching along the vortex loop as it entangles the downstream vortex.

Additionally, the extent to which the paired-vortices penetrate the main jet body seems to be less for the $AR = 3$ streamwise jet than for the $AR = 2$ case. This deviation is attributed to the thinner jet boundary/shear layer of the former as attested by the measured jet exit velocity profiles. Other than favoring the production of leading-edge vortices with smaller length-scales, it also imparts higher convective velocities upon them. These two properties were believed to have helped the paired-vortices convect faster downstream without as high an impact on the local jet entrainment as the $AR = 2$ streamwise jet, where the relatively thicker jet boundary/shear layer inevitably leads to large-scaled vortex structures as well as lower convective velocities.

In the context of achieving enhanced mixing in JICF, the regular vortex-pairing phenomenon observed here can potentially be utilised to realize further mixing enhancement by choosing the appropriate velocity ratios and allowing the mixing to be enhanced passively. This requires further investigation.

Acknowledgements

The authors are grateful for the financial supported of this research by the National University of Singapore. J. Soria would like to acknowledge the support of Monash University through a small research grant. The authors are also most grateful to Prof. T.T. Lim for his insightful illustrations of the structure of EJICF and the many fruitful discussions that were had on this research topic.

References

[1] F. Grinstein, E. Gutmark, T. Parr, Near-field dynamics of subsonic, free square jets. A computational and experimental study, Phys. Fluids 7 (1995) 1483–1497.
[2] F. Grinstein, Vortex dynamics and entrainment in rectangular free jets, J. Fluid Mech. 437 (2001) 69–101.
[3] M. Dhanak, B. de Bernardinis, The evolution of an elliptic vortex ring, J. Fluid Mech. 109 (1981) 189–216.
[4] E. Gutmark, C. Ho, Preferred modes and the spreading rates of jets, Phys. Fluids 26 (1983) 2932–2938.
[5] C. Ho, E. Gutmark, Vortex induction and mass entrainment in a small-aspect-ratio elliptic jet, J. Fluid Mech. 179 (1987) 383–405.
[6] H. Husain, F. Hussain, Elliptic jets. Part 2. Dynamics of coherent structures: pairing, J. Fluid Mech. 233 (1991) 439–482.
[7] E. Gutmark, F. Grinstein, Flow control with noncircular jets, Annu. Rev. Fluid Mech. 31 (1999) 239–272.
[8] R. Ruggeri, E. Callaghan, D. Bowden, Penetration of air jets issuing from circular, square and elliptic orifices directly perpendicularly to an air stream, in: NACA TN 2019, 1950.
[9] B. Haven, M. Kurosaka, Kidney and anti-kidney vortices in cross flow jets, J. Fluid Mech. 352 (1997) 27–64.
[10] T. Fric, A. Roshko, Vortical structure in the wake of a transverse jet, J. Fluid Mech. 217 (1994) 1–47.
[11] R. Kelso, A. Smits, Horseshoe vortex systems resulting from the interaction between a laminar boundary layer and a transverse jet, Phys. Fluids 7 (1995) 153–158.
[12] R. Kelso, T. Lim, A. Perry, An experimental study of round jet in cross flow, J. Fluid Mech. 306 (1996) 111–144.
[13] S. Smith, M. Mungal, Mixing, structure and scaling of the jet in cross flow, J. Fluid Mech. 357 (1998) 83–122.
[14] J. Blanchard, Y. Brunet, A. Merlen, Influence of a counter rotating vortex pair on the stability of a jet in a cross flow: an experimental study by flow visualizations, Exp. Fluids 26 (1999) 63–74.
[15] L. Yuan, R. Street, J. Ferziger, Large-eddy simulations of a round jet in crossflow, J. Fluid Mech. 379 (1999) 71–104.
[16] E.F. Hasselbrink, M.G. Mungal, Transverse jets and jet flames. Part 1. Scaling laws for strong transverse jets, J. Fluid Mech. 443 (2001) 1–25.
[17] E.F. Hasselbrink, M.G. Mungal, Transverse jets and jet flames. Part 2. Velocity and oh field imaging, J. Fluid Mech. 443 (2001) 27–68.
[18] A. Rivero, J.A. Ferré, F. Giralt, Organized motions in a jet in crossflow, J. Fluid Mech. 444 (2001) 117–149.
[19] L. Cortelezzi, A.R. Karagozian, On the formation of the counter-rotating vortex pair in transverse jets, J. Fluid Mech. 446 (2001) 347–373.
[20] R. Margason, Fifty years of jet in cross flow research, in: AGARD-CP-534, 1993, pp. 1–41.
[21] R. Weston, F. Thames, Properties of aspect-ratio 4.0 rectangular jets into a subsonic crossflow, J. Aircraft 16 (10) (1979) 701–707.
[22] T.H. New, T.T. Lim, S.C. Luo, A visual study on elliptic jets in cross flow, in: Proceedings of 9th International Symposium of Flow Visualisation, 2000, Paper 224.
[23] T.H. New, T.T. Lim, S.C. Luo, J. Soria, Particle image velocimetry on elliptic jets in cross flow, in: Proceedings of PIV'01, 2001.
[24] Y.-C. Cho, Digital image velocimetry, Appl. Optics 28 (4) (1989) 740–748.
[25] C. Willert, M. Gharib, Digital particle image velocimetry, Exp. Fluids 10 (1991) 181–193.

[26] J. Soria, J. Cater, J. Kostas, High resolution multigrid cross-correlation digital PIV measurements of a turbulent starting jet using half-frame-image-shift film recording, Optics Laser Technol. 31 (1999) 3–12.

[27] J. Soria, Digital cross-correlation particle image velocimetry measurements in the near wake of a circular cylinder, in: Int. Colloquium on Jets, Wakes and Shear Layers, CSIRO, Melbourne, Australia, 1994, pp. 25.1–25.8.

[28] J. Soria, An investigation of the near wake of a circular cylinder using a video-based digital cross correlation particle image velocimetry technique, Exp. Thermal Fluid Sci. 12 (1996) 221–233.

[29] J. Soria, An adaptive cross-correlation digital PIV technique for unsteady flow investigations, in: A. Masri, D. Honnery (Eds.), 1st Australian Conference on Laser Diagnostics in Fluid Mechanics and Combustion, University of Sydney, NSW, Australia, 1996, pp. 29–45.

[30] J. Soria, Multigrid approach to cross-correlation digital PIV and HPIV analysis, in: 13th Australasian Fluid Mechanics Conference, Monash University, Melbourne, 1998, pp. 381–384.

[31] K. von Ellenrieder, J. Kostas, J. Soria, Measurements of a wall-bounded, turbulent, separated flow using hpiv. Selected Papers from the 8th European Turbulence Conference, J. Turbulence.

[32] J. Westerweel, D. Dabiri, M. Gharib, The effect of a discrete window offset on the accuracy of cross-correlation analysis of digital PIV recordings, Exp. Fluids 23 (1997) 20–28.

[33] D. Hart, The elimination of correlation error in PIV processing, in: 9th International Symposium of Applications of Laser Techniques to Fluid Mechanics, Lisbon, Portugal, 1998, pp. I:13.3.1–13.3.8.

[34] M. Raffel, C. Willert, J. Kompenhans, Particle Image Velocimetry. A Practical Guide, Springer, 1998.

[35] J. Westerweel, Efficient detection of spurious vectors in particle image velocimetry data, Exp. Fluids 16 (1994) 236–247.

[36] A. Fouras, J. Soria, Accuracy of out-of-plane vorticity measurements using in-plane velocity vector field data, Exp. Fluids 25 (1998) 409–430.